

In Situ and Satellite Evaluation of Air–Sea Flux Variation near Ocean Temperature Gradients

AMANDA PLAGGE

Thayer School of Engineering, Dartmouth College, Lebanon, New Hampshire

JAMES B. EDSON

Department of Marine Sciences, University of Connecticut, Groton, Connecticut

DOUGLAS VANDEMARK

Institute for the Study of Earth, Oceans, and Space, University of New Hampshire, Durham, New Hampshire

(Manuscript received 17 July 2015, in final form 4 December 2015)

ABSTRACT

Observations of ocean–atmosphere coupling across persistent mesoscale sea surface temperature (SST) gradients are used to examine the controls of atmospheric stability, pressure gradient force, and heat flux that are considered central to oft-observed coupling between wind and SST. Moored air–sea flux measurements near the Gulf Stream are combined with QuikSCAT satellite scatterometer equivalent neutral wind (ENW) data to assess correlations between SST, air–sea fluxes, pressure, and wind perturbations at scales of 10–100 days. The net effect of ocean fronts meandering past the site enabled buoy observation of SST impacts on wind, with coupling coefficients of 0.3–0.5 similar to past studies. Wind stress–SST and ENW–SST correlation coefficients are slightly higher, and roughly 20% of the ENW perturbation is attributed to stratification impacts predicted by Monin–Obukhov (MO) similarity theory. Significantly higher correlation is observed when relating wind or stress perturbations to buoyant heat flux variation. Atmospheric pressure perturbation with SST of order $0.5 \text{ hPa } ^\circ\text{C}^{-1}$ is observed, as well as high negative correlation between wind and pressure variations. Length and time scales associated with the coupling indicate that peak correlations occur at 50–70 days and 300–500 km, consistent with mesoscale meander scales. Coupling coefficient values vary significantly depending on analysis time scale and exhibit a range near to recently observed interbasin variability. This variability is attributed to the extent of oceanic length scales permitted in the analysis. Together, results affirm the central role of SST-induced turbulent heat flux in controlling pressure field adjustments and thereby the wind perturbations over SST fronts.

1. Introduction

Ocean surface wind data from satellite scatterometers have become indispensable for applications extending from weather forecasting to climate research. A recent area of increased attention is the detection and diagnosis of air–sea coupling across SST fronts via corresponding wind field gradients seen in scatterometer data (Chelton et al. 2001; O’Neill et al. 2003, 2005, 2010a; Chelton and Xie 2010; Zhang and Busalacchi 2009). These studies

find that scatterometer-derived wind speed perturbations are related linearly to and correlated positively with mesoscale SST perturbations, with derived coupling coefficients that appear to be regionally robust but that can also change across ocean basins (O’Neill et al. 2012). However, regions of substantial SST gradients (e.g., western boundary currents, tropical instability waves, and warm and cold core rings) also frequently exhibit changing currents, atmospheric temperatures, and long waves (meanders) in the SST field (Park et al. 2006). These effects can potentially impact interpretation of scatterometer winds in such regions, because these data are considered to provide neutral stability wind estimates (e.g., Ross et al. 1985), but there is typically limited ground truth available to evaluate potential air–sea interface factors, such as surface currents

Corresponding author address: Dr. Douglas Vandemark, 8 College Rd., 142 Morse Hall, University of New Hampshire, Durham, NH 03824.
E-mail: doug.vandemark@unh.edu

and atmospheric stability and their relative importance in these process studies (Bourassa et al. 2010). Thus, interpretation of SST impacts on the overlying atmosphere and wind adjustments at varied scales when using scatterometer winds is an area of ongoing investigation (O'Neill et al. 2012; Perlin et al. 2014; Schneider and Qiu 2015).

This study attempts to investigate several facets of the SST–wind coupling phenomenon within the Gulf Stream north wall region of the northwest (NW) Atlantic using a differing but complementary approach to the spatial perturbation investigations cited above. Here we make use of a serendipitous dataset on air–sea frontal dynamics: near-surface data collected as the Gulf Stream and its meanders advected about a fixed meteorological flux measurement mooring over the course of two years during the CLIVAR Mode Water Dynamic Experiment (CLIMODE) field experiment. The strengths of these data include the ability to directly investigate wind, wind stress, pressure field, and buoyancy flux adjustments to SST change and to do so in coincidence with scatterometer measurements.

One study objective is to investigate distinctions between the wind and stress in SST coupling, in particular with respect to stability-related wind shear change across the front; this following on from the recent study of O'Neill (2012). Another is to investigate dynamics via assessment of the coupling coefficients between SST perturbations and forcing and response terms in the context of Gulf Stream meanders that impose SST variation at time scales of weeks to months within this time series dataset. Because of subtleties in the relation between scatterometer wind and surface flux buoy measurements, a brief review is provided below before the methods, results, and discussion are presented.

a. Marine atmospheric boundary layer dynamics and Monin–Obukhov similarity theory

The layer of the atmosphere above the surface of the ocean is referred to as the marine atmospheric boundary layer (MABL) because here the atmosphere is affected by friction with the sea surface, leading to turbulent air–sea exchanges of momentum, heat and mass. The region of the MABL where fluxes differ by no more than 10% is called the surface layer (or a constant flux layer), and its depth is generally the lowest 10% of the MABL. The surface layer indicates that region of the atmosphere where the flow is governed by the generation of turbulence by wind shear, and enhanced (suppressed) by buoyancy (stratification). The wave boundary layer (WBL) is the base of the surface layer where wave-induced fluctuations can impact momentum, heat, and mass exchange.

The turbulent flow statistics within most of the surface layer (i.e., outside of the WBL) can be investigated using a set of scaling arguments known as Monin–Obukhov (MO) similarity (MOS). In MOS, variables associated with turbulent flows are made dimensionless using length, temperature, humidity, and velocity scales based on the constant surface fluxes. The velocity scale u_* is the MO velocity scaling parameter, also known as the friction velocity, and is used to define the surface stress:

$$\tau = -\rho_a \overline{u'w'} \cong \rho_a u_*^2, \quad (1)$$

where ρ_a is the density of air; w' and u' represent the turbulent fluctuations of vertical wind and streamwise horizontal wind, respectively, with the overbar denoting a time average. The magnitude of the friction velocity is similar to turbulent velocity fluctuations in the surface layer.

A critical variable in turbulent surface layer definition is the vertical wind shear. In surface layer scaling, the wind shear is made dimensionless by the friction velocity and a length scale corresponding to the height above the surface. MOS predicts that the dimensionless shear is a universal function of z/L :

$$\frac{\kappa z}{u_*} \frac{\partial U}{\partial z} = \varphi_m(z/L), \quad (2)$$

where z is the height above mean sea level, L is a length scale known as the MO length, and κ is the von Kármán constant, chosen so that the dimensionless shear equals 1 in neutral conditions where $z/L = 0$. The MO length L is defined as

$$L = -\frac{\Theta_v}{g\kappa} \frac{u_*^3}{w'\theta'_v}, \quad (3)$$

where Θ_v is the mean virtual potential temperature, g is the local gravitational acceleration, and $w'\theta'_v = -u_* T_{v*}$ represents the buoyancy flux, where T_{v*} is the virtual temperature scaling parameter. The MO length represents the height at which the generation of turbulence by shear is equal to the generation of turbulence due to buoyancy. A key factor near strong horizontal SST gradients at sea is that the dimensionless shear may be strongly affected by buoyancy, which acts to enhance mixing in unstable conditions where $\varphi_m < 1$ and suppress mixing in stable stratified conditions where $\varphi_m > 1$.

MOS theory and its dimensionless functions, including $\varphi_m(z/L)$, have been validated in numerous field experiments conducted over the ocean (e.g., Edson and Fairall 1998; Edson et al. 2004, 2013), and MOS functions are widely applied in marine surface layer

investigations. For example, the dimensionless shear can be integrated to model vertical wind shear as a semi-logarithmic profile:

$$U(z) = U(z_o) + \frac{u_*}{\kappa} [\ln(z/z_o) - \psi_m(z/L)], \quad (4)$$

where z_o is the aerodynamic roughness length, and ψ_m is related to the integral of φ_m . Under neutral conditions where $z/L = 0$, the values of the stability functions are given by $\varphi_m = 1$, and $\psi_m = 0$.

The semilogarithm profile can also be used to determine the surface drag coefficient C_D required to estimate surface fluxes using bulk aerodynamic methods (e.g., [Smith 1988](#)). For example, the bulk method relates the air–sea velocity difference to the surface stress using

$$\tau = \rho_a C_D |U_r| U_r, \quad (5)$$

where C_D is the drag transfer coefficient for momentum and U_r is the vector wind speed relative to the water surface. The drag coefficient can be parameterized as a function of atmospheric stability and surface roughness (represented by roughness length z_o) by combining Eqs. (1), (4), and (5) to obtain

$$C_D(z/z_o, z/L) = \left[\frac{\kappa}{\ln(z/z_o) - \psi_m(z/L)} \right]^2. \quad (6)$$

This is the approach taken in the Coupled Ocean–Atmosphere Response Experiment (COARE) algorithm ([Fairall et al. 1996, 2003](#); [Edson et al. 2013](#)) used in this paper.

b. Scatterometer winds

The basic principles of ocean scatterometry rely on the relationship between wind waves, wind stress at the interface, and wind. Through field studies using tower-based ([Colton et al. 1995](#)), airborne ([Weissman 1990](#); [Weissman et al. 1997](#)), and previous spaceborne sensors ([Freilich and Dunbar 1999](#); [Verschell et al. 1999](#); [Weissman and Graber 1999](#)), it is generally held that the radar backscatter responds to changes in gravity–capillary waves that are, in turn, controlled by the local wind stress (e.g., [Ross et al. 1985](#); [Liu and Tang 1996](#)). Because in situ wind stress measurements are rare compared to buoy-measured winds, scatterometer vector wind geophysical models functions (GMF) are created by relating radar backscatter to ocean surface equivalent neutral wind speed (ENW) and direction, where the ENW includes compensation for stability-dependent differences between wind and stress ([Liu and Tang 1996](#)).

The concept of ENW is an extension of the wind speed relationship given by Eq. (4) in the previous section. Using this equation, and recognizing under neutral conditions $\psi_m = 0$, the ENW equation for neutral wind relative to the ocean surface U_r becomes

$$U_{rN}(z) = \frac{u_*}{\kappa} \ln\left(\frac{z}{z_o}\right). \quad (7)$$

This ENW can be related back to stress through a drag coefficient, in this case a neutral drag coefficient:

$$\tau = \rho_a C_{DN} U_{rN}^2 = \rho_a \left[\frac{\kappa}{\ln(z/z_o)} \right]^2 U_{rN}^2. \quad (8)$$

Therefore, the surface stress, and consequently ENW relative to the sea surface, is a function of the surface roughness and, to a lesser extent, air density. Studies such as [Ebuchi et al. \(2002\)](#) have validated ENW from scatterometers in an overall sense using meteorological buoy arrays such as those from the National Data Buoy Center (NDBC). Each GMF is sensor specific and takes into account the radar frequency, angles of azimuth and incidence, and polarization. Given these relationships and previous discussion, it is clear that both radar backscatter and the surface roughness to which it responds are directly related to the gravity–capillary wave field at the ocean’s surface, not to the wind field itself. Although the winds are the primary forcing on the wave surface at the length scales to which the radar responds, any additional atmospheric or oceanic processes present may also contribute to surface roughness. In this study, we assume that atmospheric stability and surface currents are first order in differentiating between ENW and the measured wind and that C_D can be taken from the COARE algorithm when deriving wind stress from the scatterometer ENW.

c. Scatterometry and SST fronts

As noted earlier, a significant number of studies have used spatiotemporally averaged scatterometer winds to investigate mesoscale wind field adjustment near SST fronts (cf. [Chelton et al. 2001](#); [O’Neill 2012](#)). [O’Neill et al. \(2012\)](#) provides an overview of the consensus and remaining questions and also includes more recent investigation of various and disparate oceanic regions (the Gulf Stream, the Kuroshio, the Agulhas Return Current, and the South Atlantic Current) with an improved methodology. One main outcome is the observation that wind speed perturbations are linearly related to and positively correlated with mesoscale SST perturbations over all four of the regions examined by [O’Neill et al. \(2010a\)](#). The aforementioned study uses 75 months of

monthly averaged spatially high-pass filtered fields of QuikSCAT wind speeds, AMSR-E satellite SST data, and the equation

$$\Delta U = \alpha_v \Delta \text{SST}, \quad (9)$$

where α_v is a linear coupling coefficient between bin-averaged wind speed perturbation ΔU and mesoscale sea surface temperature perturbations ΔSST . The authors provide α_v estimates for each of these regions, which range from $0.30 \text{ m s}^{-1} \text{ }^\circ\text{C}^{-1}$ over the Gulf Stream to $0.44 \text{ m s}^{-1} \text{ }^\circ\text{C}^{-1}$ over the Agulhas (O'Neill et al. 2012).

Previous observational studies of this coupling coefficient using satellite data have covered a wide range of spatial scales (days to months) and temporal scales (25–1000 km), as discussed by Spall (2007). The consensus result is that surface winds are enhanced over warmer water and suppressed over cooler water. A number of different mechanisms have been suggested to explain these observations, which are well summarized in Small et al. (2008). Briefly, four main mechanisms have been put forward to explain this behavior in scatterometer-derived wind field across SST fronts: 1) surface layer adjustment (SLA) of shear because of changing atmospheric stratification explained by MOS [Eq. (4)]; 2) the enhancement of vertical mixing because of cool air advection over warmer water that mixes down larger momentum from aloft on the warm side of the front; 3) the horizontal pressure and boundary layer height gradients set up by the adjustment of air temperature and humidity to the underlying SST; and 4) changes in wind stress related to changes in the relative wind due to large surface currents often associated with fronts (e.g., the Gulf Stream).

The last mechanism is more closely related to differences between the wind, wind stress, and surface current vectors rather than a coupled air–sea mechanism. Plagge et al. (2012) and others (Kelly et al. 2001; Quilfen et al. 2001) have fairly convincingly shown that scatterometer-derived winds are better correlated with the wind speed relative to the ocean U_r , than the wind speed relative to earth. Therefore, this investigation attempts to minimize the impact of currents in our analyses by using the buoy-measured currents to produce relative winds in this study. The first mechanism is almost certainly present for wind flowing across the horizontal SST gradient; in essence this surface layer adjustment is predicted a priori by MOS. The only question then is how closely does MOS fit with the absolute magnitude of the observed versus predicted ENW changes, and how well can this be validated with the limited MABL data available in most studies? Next, numerous observational and numerical studies have

concluded that boundary layer adjustments (BLA) due to mechanisms 2 and 3 are both occurring at large spatial scale [$O(100)$ km] across SST gradients with derived wind perturbations that significantly exceed surface-driven change alone. Thus, perhaps the more central debate lies in determining the relative importance of these mechanisms to control of the observed correlation between SST and wind speed (Small et al. 2008). This study attempts to use direct covariance air–sea flux data collected in the dynamic MABL of the Gulf Stream north wall region to shed further light on this debate as well as to further clarify the contribution of SLA to this coupling coefficient.

2. Data and methods

The region of interest for this study centers on an air–sea flux measurement buoy moored near the Gulf Stream north wall (see Fig. 1) as part of a field experiment conducted from November 2005 through January 2007. CLIMODE was conducted to investigate the formation and subsequent evolution of subtropical North Atlantic Mode Water (Marshall et al. 2009). Of particular importance in the mode water formation is the advection of cold, dry air from the wintertime continent out over the warm Gulf Stream and north wall meanders during such cold air outbreaks. The airflow can drive extremely high sea-to-air latent and sensible heat fluxes because of large interfacial temperature and humidity differences and also because of the strong winds typically associated with these events. This then drives intense convective activity and strong vertical exchange of both moisture and heat with combined values of the latent and sensible heat flux often exceeding 1000 W m^{-2} (Marshall et al. 2009). The present study makes use of data from these cold air outbreaks but also all data from over the entire buoy deployment where two features of the dataset are most critical. First, over the course of 14 months both Gulf Stream north wall instabilities (warm core eddies or meanders) as well as seasonal zonal migration of the mean stream position effectively allowed the fixed CLIMODE buoy to sample both warmer in-stream and colder external waters. The resulting fixed mooring dataset provides an effective spatial SST gradient measurement. Second, the large range of atmospheric boundary layer stability that occurred over the buoy as well as the large range of in- and out-of-stream surface currents combined to provide dynamic range within the time series that can help to distinguish wind stress from the wind. The distinction may help to better evaluate the coupling between near-surface wind, wind stress, and horizontal SST gradients and may also apply to the interpretation of satellite

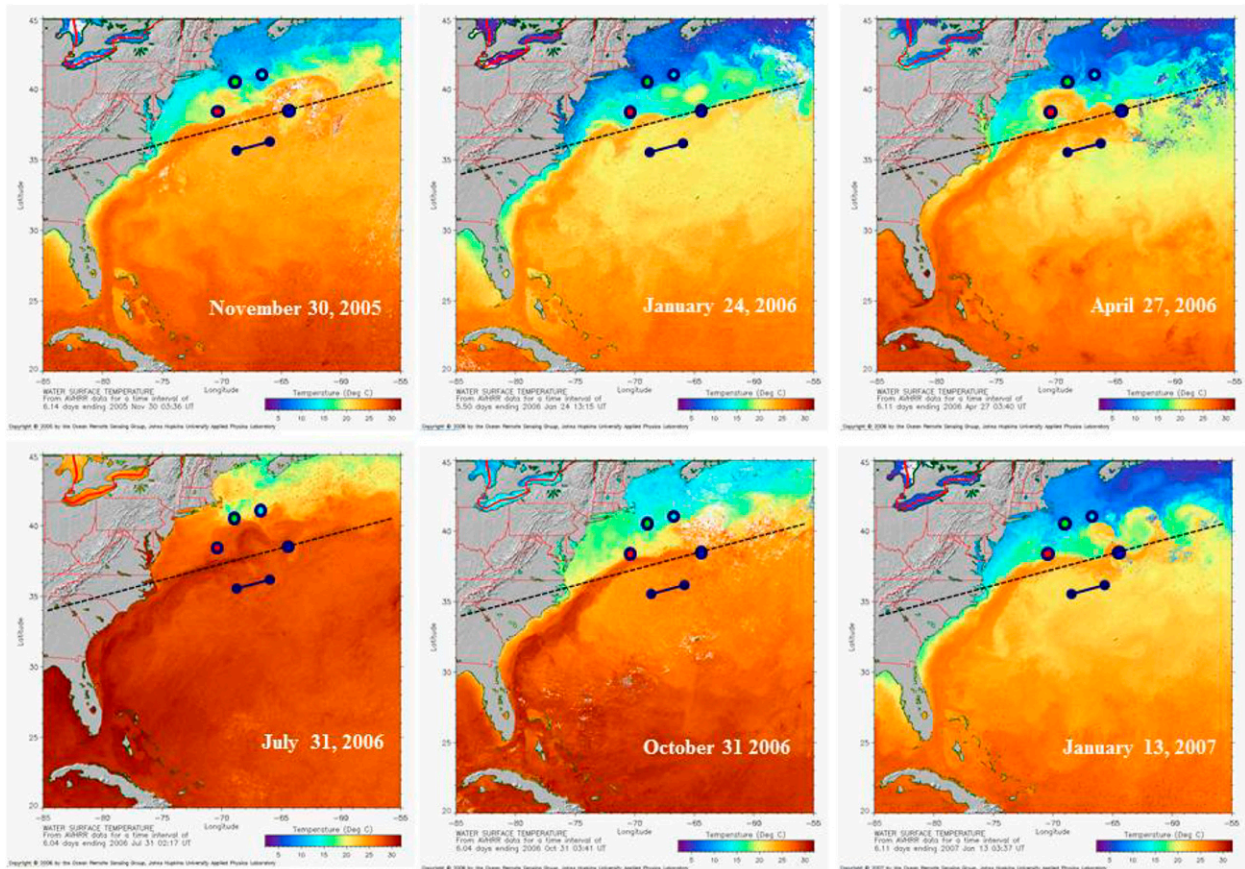


FIG. 1. Sequential maps off the U.S. East Coast showing SST variability as measured from the AVHRR from November 2005 to January 2007. The large blue circle shows the CLIMODE DCFS buoy location and central study site, while the dashed line gives the average orientation of Gulf Stream northern wall. The other circles represent 2006 locations for NDBC buoys 44004 (red), 44008 (green), and 44011 (cyan). The dumbbell indicates a distance of 330 km representing the typical wavelength of Gulf Stream meanders. The satellite imagery is courtesy of the Ocean Remote Sensing Group of Johns Hopkins University Applied Physics Laboratory.

scatterometer ENW when combined with buoy wind stress data.

The primary in situ dataset used in this investigation was collected on a 2.7-m met-ocean discus buoy that served as the central air-sea flux time series platform for CLIMODE. A detailed description of the buoy design, deployment, and measurements are provided by Weller et al. (2012) and Bigorre et al. (2013). Briefly, the buoy supported two separate Air-Sea Interaction Meteorological Systems (Hosom et al. 1995) to provide redundant measurement of wind speed and direction, air temperature, humidity, barometric pressure, rainfall accumulation, and downwelling longwave and shortwave radiation. Below the buoy, near-surface current vector, water temperature, and salinity were each measured hourly. Fluxes of momentum and buoyancy were computed using a low-power version of a direct covariance flux system (DCFS; Edson et al. 1998). The DCFS comprised a three-axis ultrasonic anemometer-thermometer for velocity and

sonic temperature measurements, a strapped-down inertial sensing system to record platform motion (providing three-axis accelerations and angular rates), and a compass for heading. The sonic temperature closely approximates virtual temperature (Larsen et al. 1993), and its correlation with the vertical velocity can be used to compute the buoyancy flux. The high-rate (20 Hz) DCFS data are used to compute hourly 20-min estimates of momentum and buoyancy fluxes using the direct covariance (or eddy correlation) method after correcting for platform motion (Edson et al. 1998; Miller et al. 2008). The combination of scalar and eddy correlation measurements then permits calculation of the wind, stability, and wind stress estimates of Eqs. (1)–(8) via both bulk and direct covariance methods. Where bulk methods are used, we apply COARE 3.5 algorithms. The collection of long-term direct covariance flux measurements and current-corrected winds in tandem with scatterometer winds is uncommon and will be assessed in the next sections.

The study also takes advantage of three nearby NDBC buoys (NOAA/National Data Buoy Center 2012) located northeast (NE) of the CLIMODE region, as shown in Fig. 1. Two of these buoys are located to the north of the Gulf Stream. The westernmost buoy 44004 is occasionally located within north wall meanders, as shown by the spatial structure of the SST field in Fig. 1 (and the sea temperature time series in Fig. 3). These Gulf Stream meanders result in sea temperatures at the westernmost buoy that can be warmer than at the CLIMODE buoy because of the spatial structure of the eddy field. This is discussed further in section 3.

The satellite scatterometer data considered here are from the QuikSCAT sensor, specifically the 12.5-km resolution L2B QuikSCAT version 2 product from NASA JPL's Physical Oceanography Distributed Active Archive Center (SeaPAC 2013). We have checked results using recent QuikSCAT version 3 data processing and find no significant alteration of study conclusions. The QuikSCAT orbit and swath provided twice daily coverage of the study region. The process for collocating in situ and QuikSCAT data both spatially and temporally is documented in previous work (Plagge et al. 2009). Briefly, for a successful collocation pairing, wind observations between the buoy and scatterometer must occur within 30 min of each other. For each satellite pass within this time frame, all scatterometer wind estimates, or wind vector cells (WVC), within a 10-km radius of the buoy have been averaged to provide a single wind speed and direction estimate. We discard any WVC that has been flagged as contaminated by rain. With the exception of a few outliers, there is good agreement between QuikSCAT wind speed and in situ surface-relative wind speed, as shown in Fig. 2. Figure 2 includes both the buoy-measured wind and ENW (U_{10N}), both adjusted to a 10-m height. Close inspection indicates better agreement between the QuikSCAT and ENW. That agreement is further quantified in section 3.

3. Results

Using both buoy and satellite datasets, the following results focus on wind speed variation within this region characterized by proximity to strong SST fronts. Direct measure of the turbulent fluxes and pressure by the CLIMODE platform allows exploration of the adjustment of the surface layer winds and stress to the underlying SST through a substantial range of z/L . The investigation is aided by the long data collection window, allowing an investigation of the temporal response of wind speed and surface stress to variability in the SST and heat fluxes on weekly to seasonal time scales.

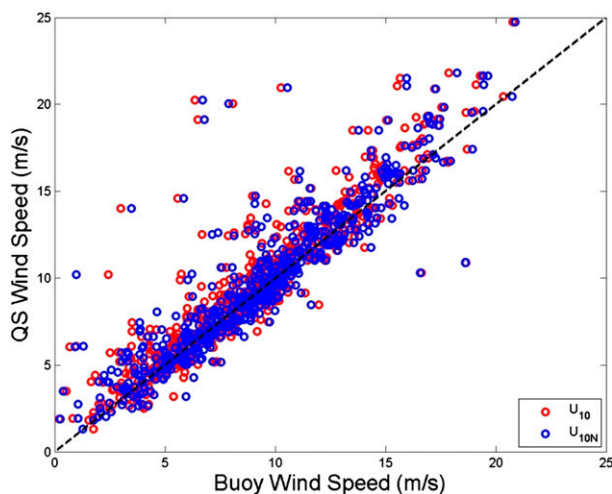


FIG. 2. Scatterplot showing collocated QuikSCAT vs buoy wind speeds for the entire dataset ($N = 581$). The red circles represent direct measurements of the wind adjusted to 10 m. The blue circles represent buoy data that have been adjusted to estimate the wind speed at 10 m under neutral conditions. Both buoy wind estimates have been adjusted for surface current and thus represent wind speeds relative to water.

a. Surface layer adjustment

Given questions that have arisen surrounding controls on wind adjustment across SST fronts, we first examine the extent to which one observes that the scatterometer winds are more closely aligned with equivalent neutral wind rather than the unadjusted “true” value. This can be assessed in Fig. 3, which shows the observed ratio between QuikSCAT and measured winds and that between the neutral and measured winds, both as a function of z/L . The stability range spans from strongly unstable ($z/L \approx -1$) to strongly stable ($z/L \approx 0.5$). Although it is difficult to discern from the individual point measurements, the bin-averaged results versus z/L indicate that both satellite and the buoy neutral winds show similar offsets from the measured or true wind. Scatter is not unexpected, as MOS is not supposed to collapse these results as a function of z/L . For example, MOS predicts that the wind speed difference is given by

$$U_N(z) - U(z) = \frac{u_*}{\kappa} \psi_m(z/L). \quad (10)$$

Therefore, variability in u_* (i.e., variability in wind shear and surface stress) will lead to variability in the wind speed difference for any given stability level. The bin averaging is expected to provide results for the average value of u_* for conditions at the buoy versus the average value of the conditions in the QuikSCAT footprint around the buoy. Indeed, we observe overall agreement between the bin-averaged results that clearly

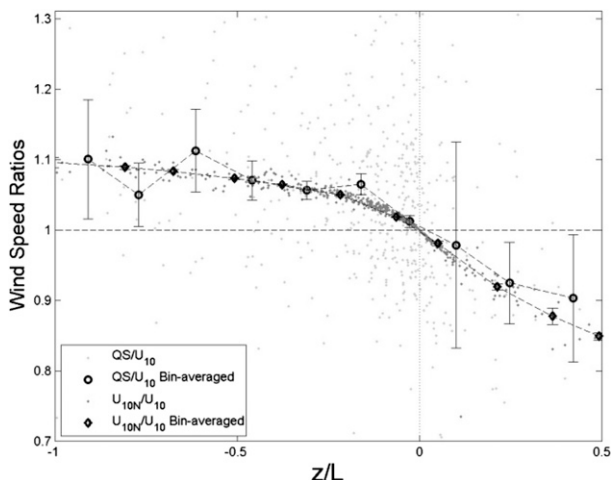


FIG. 3. Plot of the ratio of neutral stability against measured wind vs z/L . Black dots indicate buoy-neutral winds over buoy-measured winds; gray dots indicate scatterometer wind over buoy-measured wind. Binned averages for black dots are indicated by the black diamonds connected with a solid line, and binned averages for the gray dots are indicated by the circles connected by the broken lines. The error bars indicate the standard error of the data with each bin.

differentiate both the buoy and satellite ENW from the nonadjusted measurements and that the close agreement between these two ENW estimates across the full range of z/L indicates that the satellite ENW data are adhering quite well to the MOS model within this dataset. Figure 3 ratios indicate 10% increase in neutral versus actual winds for unstable conditions and a slightly larger decrease in stable conditions, close to that predicted by MOS using COARE.

Using these results, one can predict that such surface layer wind adjustment due to atmospheric stability controlled by the ocean across an SST gradient could amount to a 5%–20% change in ENW. For example, consider advection southward and a transition from a neutral MABL to an unstable layer over warm Gulf Stream water. Values in Fig. 3 suggest that the ENW will increase by approximately 0.5 m s^{-1} over the warm water for a wind of 5 m s^{-1} . The opposite effect would be seen for an air mass moving from warm to cold. The maximum perturbation would be close to 20%.

Such changes in near-surface stability for airflow from cool to warm or warm to cool is the basis for why SLA is expected to induce a positive coupling coefficient between ENW and SST in Eq. (9) even if the actual wind remains constant. In most cases, determining the extent of SLA impact on this coupling coefficient requires knowledge of the horizontal variability in both the wind speed and SST. This can be further complicated by the surface currents and thermally driven processes that drive variability in both the ENW and true wind speeds.

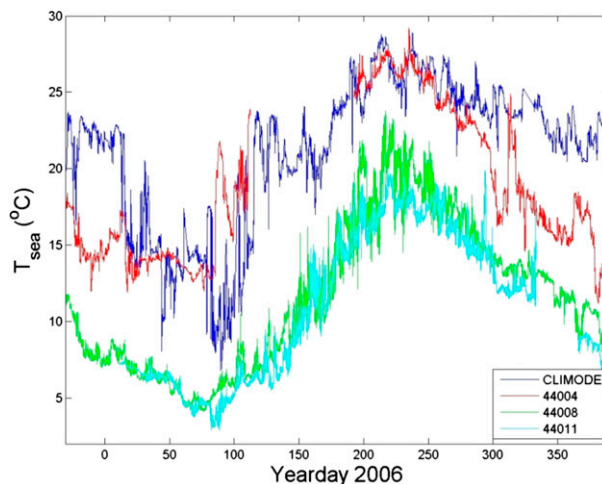


FIG. 4. Time series of near-surface sea temperature measurements from the four buoys used in this analysis. The location of these buoys is shown in Fig. 1, and the colored symbols match the color of the line used for the time series.

These processes and SLA contributions are further investigated in the following sections, but we note that the first-order surface current impacts on wind and ENW should already be removed because of the use of observed water-relative velocities.

b. Wind velocity–SST coupling observed between paired moorings

Next, a regional estimate of the relationship between wind perturbations and SST perturbations (ΔSST) is derived following the approach of O'Neill (2012) and using paired buoy measurement differences among four sites shown in Fig. 1 to determine the coupling coefficient of Eq. (9). The wind and SST differences are spatial and computed across distances of 100–200 km in this case, while in the following section an alternate temporal derivative approach for computing ΔSST and ΔV is taken using solely the CLIMODE mooring data. Significant differences in the SST between stations are observed over the annual cycle, as shown in Fig. 4. The northernmost buoys are always found in the cooler shelf water and agree to within a few degrees of each other over the year. This contrasts with the two southernmost buoys that show significant variability over shorter time scales. This is because of the proximity of these buoys to the northern wall of the meandering Gulf Stream. For example, the CLIMODE buoy was originally deployed (late 2005) in warm Gulf Stream waters well south of the northern wall. By January, however, the buoy was in cooler water just north of the wall as a result of a Gulf Stream meander. In late March through April, the westernmost NDBC buoy (44004) was in warmer water

than the CLIMODE buoy because of a Gulf Stream ring that propagated west to this station.

Our buoy-difference calculations do not reproduce the rigorous analysis of O'Neill (2012), in part because the focus is on a smaller region of interest as well as a shorter 15-month time period when the CLIMODE buoy was deployed. Rather, here we only compute the coupling coefficient between the measured winds and SST (i.e., ENW and wind stress are not addressed in this subsection), and the winds are only corrected for surface currents at the CLIMODE mooring. However, the inclusion of the CLIMODE mooring does provide an additional complete time series near to the warmer surface waters associated with the Gulf Stream for comparison with three of the buoys used in O'Neill (2012), as well as gradients between two buoys at the edge of the meandering Gulf Stream (i.e., the CLIMODE buoy and NDBC 44004). As such, it provides some test of the consistency with relationships found in O'Neill (2012) near to and north of the Gulf Stream region.

Similar to the processing and quality control steps taken in O'Neill (2012), individual measurements and differences in the wind speed and SST between buoy pairs that exceed three standard deviations from their 30-day running means are removed. The time series are then smoothed using a 10-day running average to filter out synoptic weather disturbances. Wind speed and SST perturbations are defined as the computed difference between the CLIMODE mooring and each of the 3 NDBC buoys. These perturbations between the CLIMODE and NDBC buoys are then bin averaged according to the SST gradient, as shown in Fig. 5. A linear fit to the bin-averaged data provides an estimate of the coupling coefficient of Eq. (9). The least squares regression yields a slope and 95% confidence interval of 0.19 ± 0.04 and a correlation coefficient of 0.92. The y intercept of the line for the three buoy pairs is -0.32 m s^{-1} . The slope is in good agreement with the average value of 0.22 reported by O'Neill (2012) for his Gulf Stream region analyses. Note that all of the negative values of ΔSST are a result of differences between the CLIMODE buoy and the westernmost NDBC buoy when it was in warmer water because of a Gulf Stream ring. All three buoy pairings contribute data with positive values of ΔSST .

c. Velocity–SST coupling derived using only the CLIMODE mooring

Referring to the significant SST variations in time observed at the CLIMODE buoy (Fig. 4) and their likely attribution to known Gulf Stream meanders and filaments (Fig. 1) near the buoy's north wall location, we

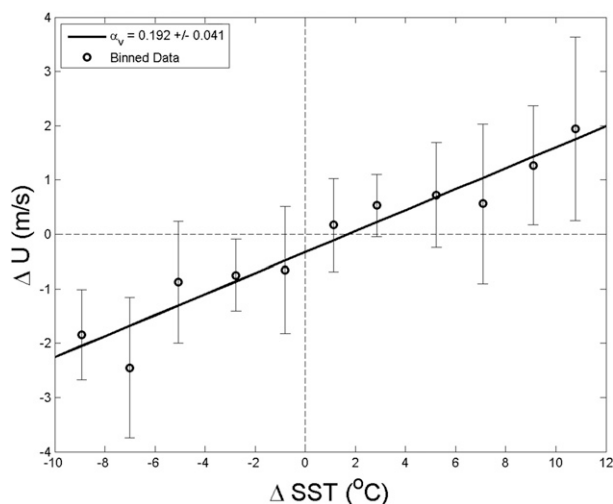


FIG. 5. Wind speed perturbations between buoy pairs (CLIMODE–NDBC) binned according to ΔSST , where the bin size is 2°C . The error bars represent the standard deviation about the mean for each bin. The solid line is a fit to the data shown with a slope of $0.19 \text{ m s}^{-1} \text{ }^\circ\text{C}^{-1}$, a y intercept of -0.032 m s^{-1} and a correlation coefficient of 0.96 ($R^2 = 0.92$).

investigate an alternative approach for examining wind–SST coupling by using data collected at a fixed location. In essence, we now substitute observed time variability for the spatial gradients in the SST, wind, and other diagnostic variables that have been addressed in past studies of SST-induced MABL dynamics. The analysis closely follows the method described by O'Neill (2012), where the key change is the use of temporal perturbations about running means from our single buoy rather than spatial perturbations between buoy pairs. First, bandpass filtering is applied to the 15-month-long time series collected on the buoy. As in O'Neill (2012), a 10-day running averaging (i.e., low-pass filter) is applied to remove synoptic-scale variability in all time series from here forward in this study. The low-pass filtered SST time series is shown by the red line in Figs. 6a and 6c. Next, a high-pass filter is applied that consists of the subtraction of a longer-time-scale running mean signal from the low-pass filtered signal. To illustrate, blue lines in Figs. 6a and 6c, respectively, represent the 30- and 90-day SST running means. The differences between the red and blue lines are shown in Figs. 6b and 6d. These are time-variant SST perturbations (ΔSST) from the bandpass filtering of the raw SST time series. Using an identical approach for wind, the 10-m buoy wind speed perturbation (ΔU_{10}) is shown by the blue lines in Figs. 6b and 6d.

Examination of ΔSST and ΔU_{10} data of Fig. 6 does suggest qualitative coherence between the wind and SST perturbations with either the 30- or 90-day filtering.

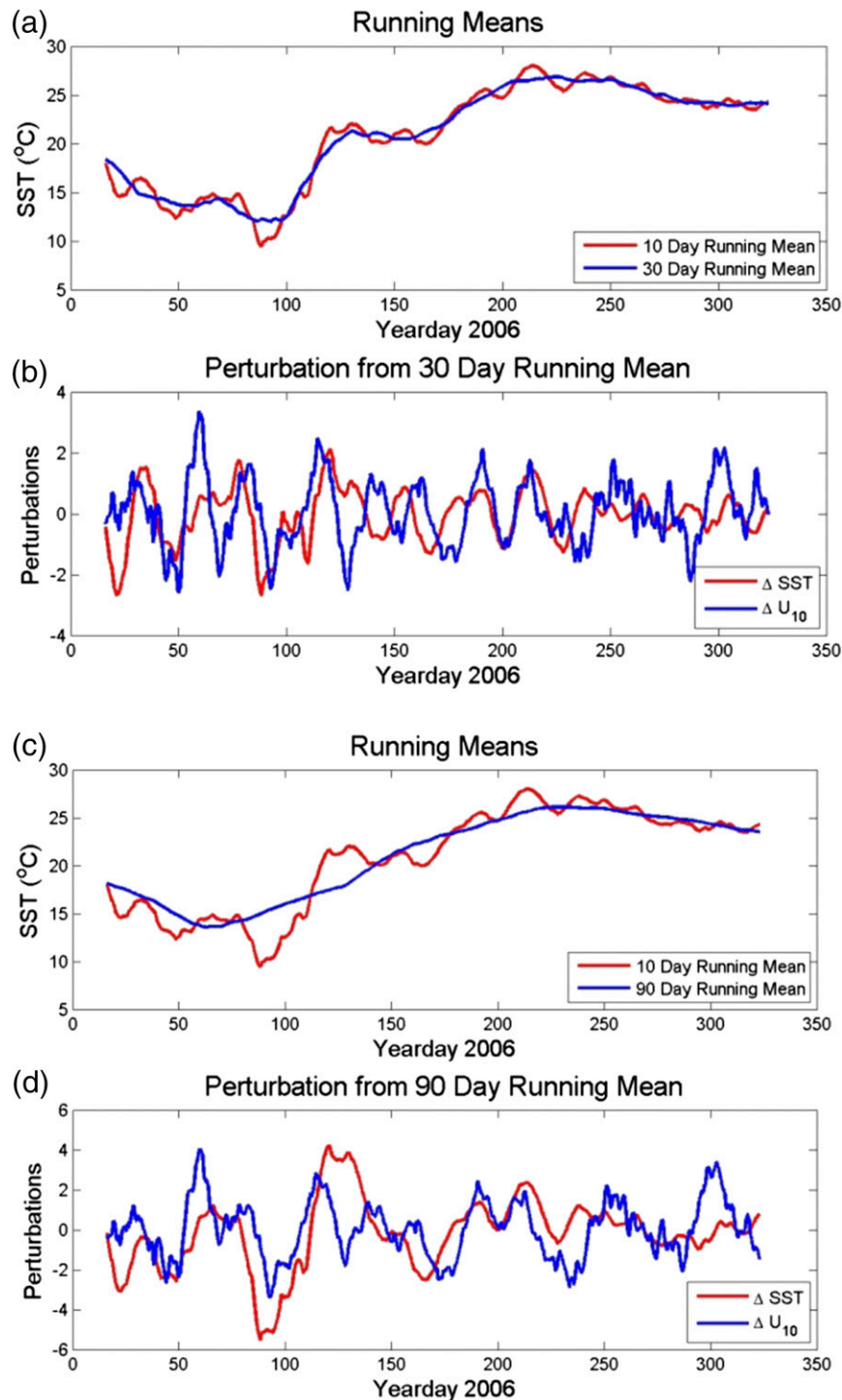


FIG. 6. Two temporal perturbations examples computed from 30-day or 90-day running means. (a) The 10-day low-pass filtered SST time series (red) and the 30-day running mean (blue). (c) As in (a), but for 10 and 90 days. Also shown are the (b) 30-day and (d) 90-day band-passed filtered time series for Δ SST [i.e., the difference between these two lines in (a); red] and 10-m wind speed ΔU_{10} (blue; generated using the same procedure).

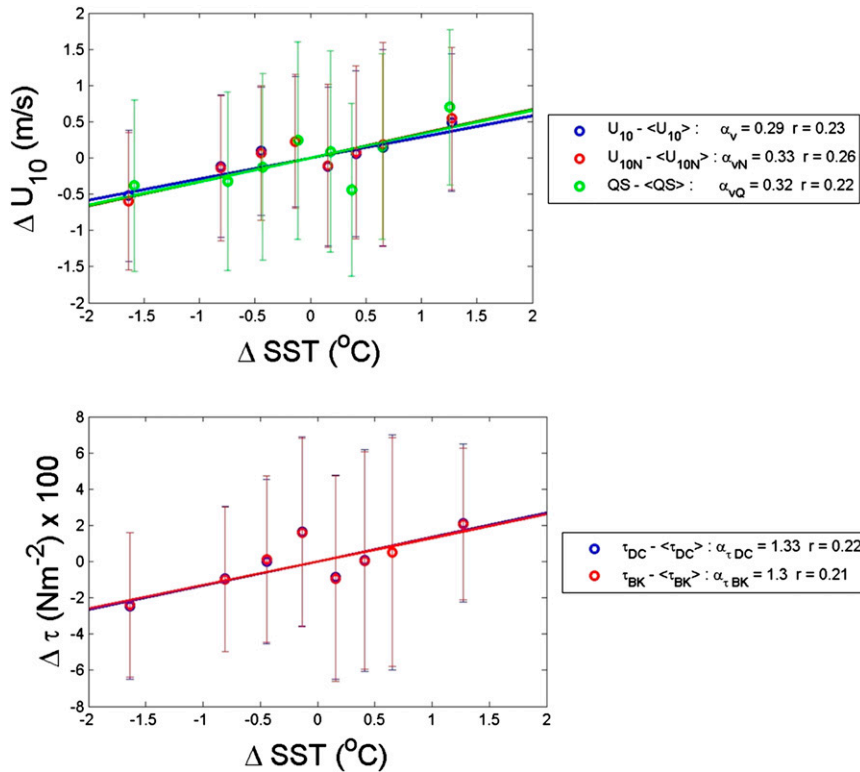


FIG. 7. (top) The coupling coefficients for measured, neutrally adjusted and QuikSCAT winds and (bottom) the coupling coefficient for the measured and bulk-derived surface stress. Respective time series are high-pass filtered using a 30-day running mean. The bin averages are computed using an equal number of points in each bin. The symbols and uncertainty bars represent the bin mean and standard deviations. The lines are least squares fits to the data assuming a zero intercept. Coupling coefficients are determined from the slope.

Given the interest in the atmosphere–ocean coupling carried in the wind–SST relationship, we next compute a coupling coefficient between SST and wind speed time residuals. Using the overall dataset, the computation is made for U_{10} and U_{10N} for the buoy as well as for the collocated ENW from QuikSCAT. The results for wind speed versus SST perturbations when using a 30-day running mean are shown in the top panel of Fig. 7. The coupling coefficients ($\alpha_{vN} = 0.33$ buoy and $\alpha_{vN} = 0.32$ QSCAT) derived in this manner are in close agreement with the North Atlantic value of $\alpha_{vN} = 0.30$ reported by O’Neill et al. (2012), with near equivalence between the scatterometer and buoy-derived U_{10N} results.

A similar analysis can be conducted for any of the meteorological variables measured at the buoy; key among these is the coupling coefficient between SST and wind stress perturbations. Results are provided in Fig. 7, where the coupling coefficient derived from perturbations obtained from both the direct covariance (DC) and bulk aerodynamic (BA) surface stress time series are shown. Again, the values of the coupling coefficient for the wind stress, $\alpha_{\tau} \approx 1.3$, is in good agreement with the

value of $\alpha_{\tau} = 1.4$ reported by O’Neill et al. (2012). The linear regression correlation coefficients R between SST and wind speed and SST and wind stress are noted in Fig. 7 and are nearly statistically equivalent. This is consistent with O’Neill et al. (2012), who provide an analytical argument [see their Eqs. (6) and (7)] that predicts a nearly equivalent relationship between τ –SST and U_{10N} –SST perturbations over the length (time) scales of atmosphere–ocean coupling and the magnitude of the wind perturbations that underlie these analyses.

d. Temporal and spatial scales of the coupling

The quantitative agreement between results produced in the previous section using time variable data at the CLIMODE station and results from many previous studies that use direct assessment of the spatial gradient fields of SST and wind implies that there was sufficient oceanic advection about the buoy site to effectively create a type of Lagrangian measurement framework: one that permits sampling sufficient to obtain results that are consistent with an observed SST-induced secondary circulation. As noted in several studies (cf. Small

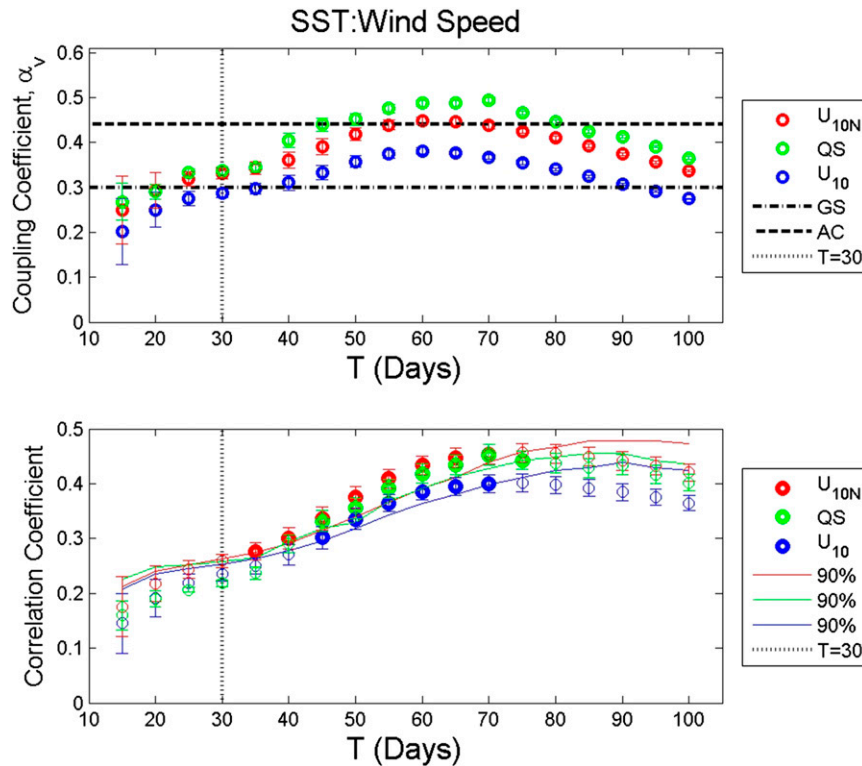


FIG. 8. Correlation between SST and wind perturbations as a function of running average time used in the high-pass filter. The wind speeds represent the true wind speed at 10 m (blue), the neutral value adjusted to 10 m (red), and the satellite wind from QuikSCAT (green). The symbols and uncertainty bars represent the mean and standard deviation of the values found by varying the time scale used in the low-pass filter between 8 and 12 days. (top) The broken lines represent the mean values found over the Gulf Stream (GS) and the Agulhas Current (AC), as reported in O'Neill et al. (2012). The vertical dotted line corresponds to $T = 30$ days, as also shown in Fig. 7. (bottom) Solid curves represent the value of the correlation coefficient at the 90% confidence level.

et al. 2008), there are several physical processes that likely contribute to this observed linear coupling between wind and the SST at the oceanic mesoscale but also to an observed and unexplained range of variation in the absolute value of α_v among ocean basins that can span between 0.3–0.44 (O'Neill et al. 2012) and 0.21–0.41 among buoy pairs in the NW Atlantic Gulf Stream region (O'Neill 2012). The present time series data approach may provide additional information on this issue by exploiting the potential to examine variation in α over time scales of weeks to months in the region under study. To address this, the low-pass running means used to extract the perturbation time series are now varied between 15 and 100 days. We define a temporal length scale T , where T is the duration or cutoff (in days) defined by the high-pass filtering applied to these time series. The same 10-month period is used to compute the correlations among scalars using only the first CLIMODE buoy deployment dataset. This allows a

better comparison between results at all temporal scales from 10 to 100 days and avoids the issue of a gap that exists between the first and second buoy deployments. Coupling coefficients are determined by a least squares fit to the data (i.e., the same procedure used to calculate the $T = 30$ day result shown in Figs. 6 and 7).

Results are shown in Fig. 8 and provide a measure of α as a function of T . It becomes obvious that both this slope and the correlation coefficient (bottom panel) of the wind–SST relationship vary by nearly a factor of two and generally increase with time duration to a local maximum near $T = 60$ – 70 days. The symbol and uncertainty bars in Fig. 8 represent the mean and standard deviation of the values found by varying the low-pass filter used in the analysis between 8 and 12 days where the correlation coefficients were found to converge. This is consistent with the findings reported by O'Neill (2012), who used similar smoothing to attenuate the atmospheric synoptic scale. The North Atlantic value of

$\alpha_{vN} = 0.30 (\pm 0.05)$ reported by O'Neill et al. (2012) used temporal averaging that corresponds to filtering using a 30-day running mean ($T = 30$), as indicated by the vertical line in Fig. 8 (and results in Fig. 7a). Overall, when comparing Fig. 7a to results in Fig. 8 at $T = 30$, one sees consistency in values of α and in correlation coefficients.

The lines shown on the bottom panel of Fig. 8 and again in Figs. 9 and 10 are computed to help gauge statistical significance at the 90% level for the linear correlation coefficients. They represent the correlation levels that could be achieved in 10% of cases where the two time series under test are random (null hypothesis). These levels are computed following Emery and Thomson (2001), with the effective degrees of freedom N_{eff} computed using the method described by Chelton (1983). The maximum lag used to integrate the correlation functions is set to 30% of the time series (or approximately 100 days), as described by Pineda and Lopez (2002) and Whitney and Garvine (2006). The symbols are shown in bold if values exceed significance levels of 90%. Using that measure, the correlation between SST and the buoy neutral wind speed perturbations are significant for mean periods between approximately 35 and 65 days. But the p test does not disqualify the results at short and longer time scales; it merely indicates the R values have slightly less confidence ($\sim 85\%$). This also applies to the results of Fig. 7 at $T = 30$ days shown in Fig. 7. Moreover, in recent studies of SST to wind coupling (O'Neill 2012; O'Neill et al. 2012), large datasets have been assembled to confirm that correlation coefficients on the order of 0.2–0.5 are not a statistical artifact.

Note that the coupling coefficient for U_{10N} (or ENW) is consistently higher than U_{10} (i.e., the measured wind) by approximately 20% at all T . This increase and its magnitude are consistent with what one expects from the surface layer adjustment discussed in section 5a, and also with that observed in Fig. 7a. As shown already, QuikSCAT winds are expected to closely approximate ENW, and indeed the QuikSCAT-derived coupling coefficients shown in Fig. 8 indicate that the satellite winds actually indicate equal or greater wind–SST coupling levels than levels obtained using buoy U_{10N} .

It is also of possible interest to note that the observed range of variability in the U_{10N} coupling coefficient with time scale in Fig. 8 is roughly bounded by the differing coefficients found near the Gulf Stream and Agulhas Current, as reported in O'Neill et al. (2012), where 30-day averaging and spatial high-pass filtering was used. Here it is not the region that is changing, merely the extent of the time scales of signal permitted into the correlation analysis. One speculation is that the longer time scale allows the more energetic signals associated

with advecting Gulf Stream meanders to enter into the perturbation time series. This suggests that the value of the coupling coefficient may be changing as a function of the dominant scale of mesoscale SST variability. This idea has some merit: for example, if one combines the finding in O'Neill et al. (2012) that α_{vN} increased from west to east along the Gulf Stream extension with the study of Lee and Cornillon (1996; see their Fig. 7), who analyzed Gulf Stream meanders to show that their amplitude, period, and length scale also increase west to east and that a 45-day period represents the median of the most energetic meanders along the north wall.

e. Further investigation via dynamical response variables

It is assumed in this and previous studies that mesoscale SST gradients serve as the primary control for the observed atmospheric stratification and horizontal adjustment of the wind field. This is true whether the actual cause for observed wind gradient is 1) surface layer adjustment due to changing surface stratification explained by MOS; 2) vertical momentum exchange due to cool air advection over warmer water that mixes down larger momentum from aloft; and/or 3) the horizontal pressure gradient set up by the adjustment of air temperature and humidity to the underlying SST. Our flux measurement platform provides several additional measurements that may help to shed light on the relative role of these processes within this study region and timeframe.

First, the analysis can be extended to compute the correlation between surface level wind variation and coincident perturbations in the sea–air virtual temperature difference $\Delta(\Delta T_v)$, as well as in the measured buoyancy heat flux (BHF) $\Delta(\rho c_p w' \theta'_v)$. These two quantities are known to more directly define thermally driven ocean–atmospheric adjustment processes in comparison to a proxy like the ocean temperature gradient, and we anticipate that the wind perturbations induced by SST change are ultimately, and more closely, coupled to these SST-induced perturbations. Results, shown in Fig. 9, are quantified in terms of correlation coefficients that can be compared directly to Fig. 8. As expected, a first obvious difference is that covariance is markedly elevated with respect to the SST–wind coupling shown in Fig. 8b. The increase in R is nearly a factor of 2 for both the air–sea temperature difference and BHF and for any time scale T . Highest correlation is seen between the buoyancy flux and the wind.

A separate observation in Fig. 9 is an increase in R levels when using U_{10N} rather than U_{10} , equivalent to that seen when using SST, and consistent with wind stress ($\sim U_{10N}$) adjustment being partly attributed to

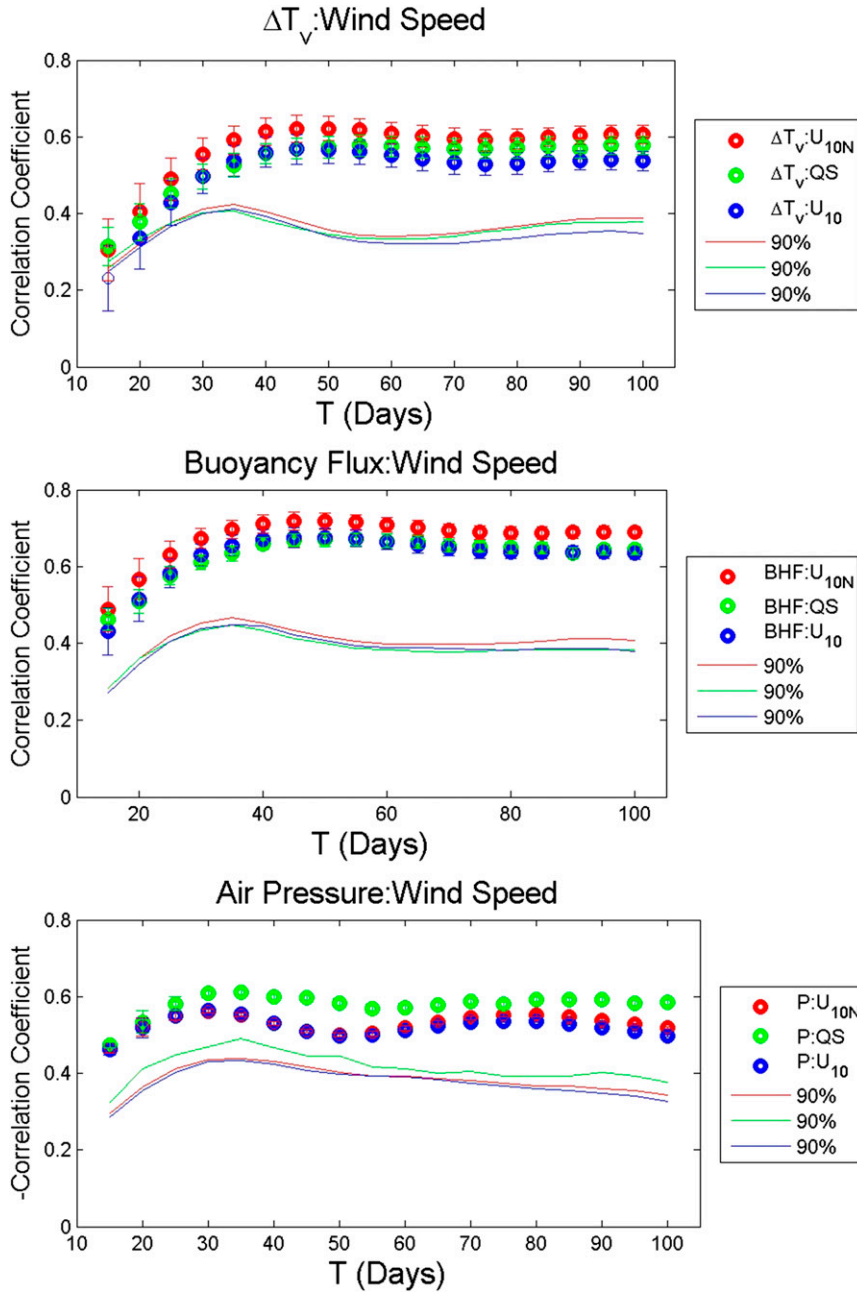


FIG. 9. The correlation coefficients between perturbations in winds with (top) those in the sea–air virtual temperature difference, (middle) buoyancy heat flux, and (bottom) atmospheric pressure as a function of T . Note that the correlation is negative in (bottom). The symbols and uncertainty bars are the same as those shown in Fig. 8. The lines show the value of the correlation coefficient at the 95% confidence level for (top) and 99% for (bottom). Symbols in bold indicate values above these levels.

surface layer stability change as discussed above. Another indication of more direct coupling is that all computed wind cross correlations calculated with the buoyancy flux perturbations are statistically significant for $p < 0.01$.

A second aspect of the dynamics that can be investigated with these data is found in the surface level pressure and wind stress perturbations as shown at the bottom of Fig. 9 and then in Fig. 10. Pressure changes in Fig. 9 are shown to be significantly and negatively

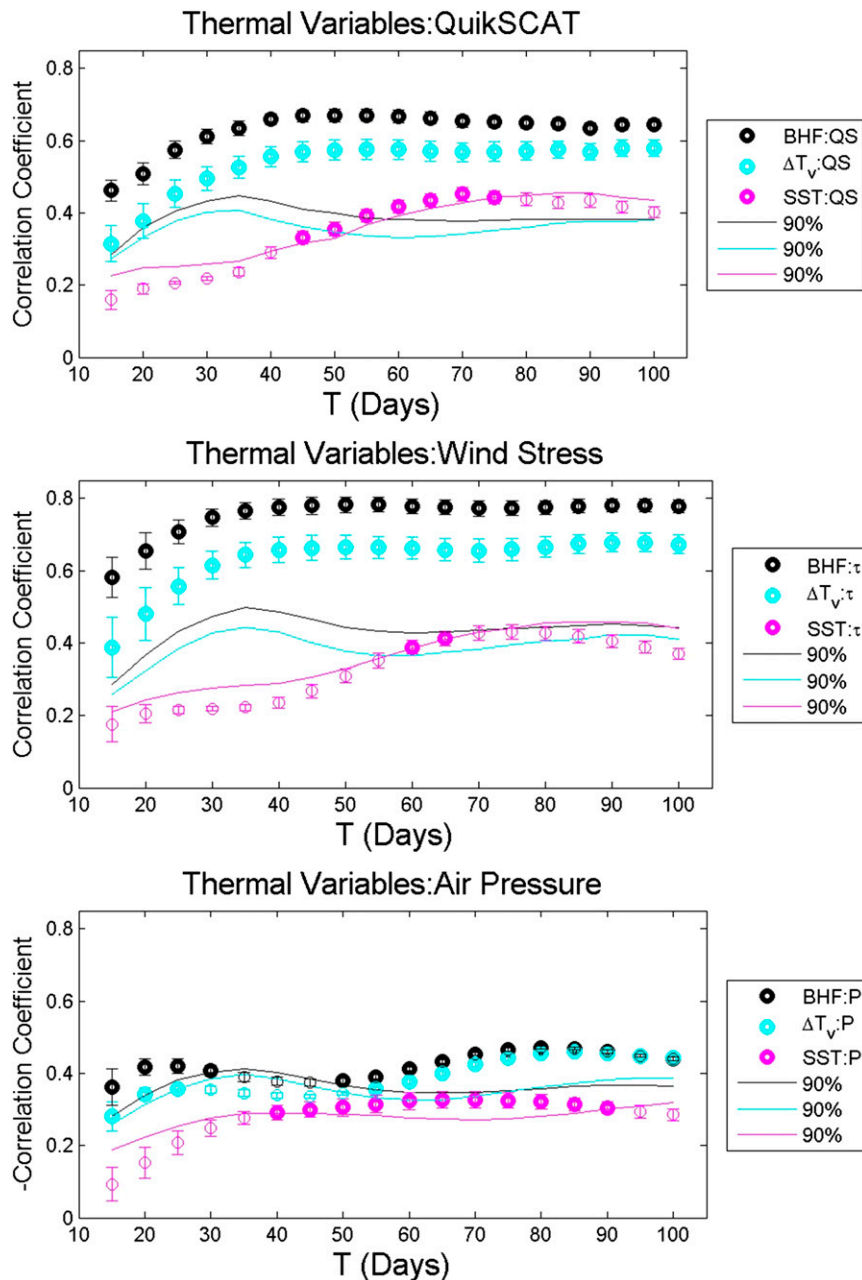


FIG. 10. (top) The correlation coefficients between temporal QuikSCAT wind perturbation and perturbations in SST, sea-air virtual temperature difference, and buoyancy flux as a function of time series filtering; (middle) as in (top), but for wind stress; (bottom) as in (top), but for the anticorrelation with surface level pressure. The lines in (top)–(bottom) represent the level for statistical significance at the indicated value of confidence. Symbols in bold indicate values above these levels.

correlated with the wind field regardless of wind product and at a level between -0.45 and -0.6 for all T .

Results of Fig. 10 document the strength in the linear relationship observed when one relates a response change in wind, stress, and pressure to the variation in SST, the sea-air temperature difference, or buoyancy

heat flux. Inspection of the relative magnitude change for any time T within each panel shows an increase in correlation as one progresses through these latter three thermal control variables for all three response factors. The largest correlation is seen between the BHF and wind stress (middle panel), a value slightly greater than

for that seen between BHF and QuikSCAT wind. The correlation between SST and wind stress is less than half that for BHF–wind stress and significant only for T near 60 days. The magnitude of their respective anti-correlations with the pressure perturbations are lower, all falling below 0.4 and most significant only near T of 60–80 days.

Additionally, the increase in the negative correlation between P and ΔT_v , and between P and the buoyancy flux shown in Fig. 10, is smaller than the increase seen in the positive correlation between wind speed and these parameters shown in Fig. 9. The increase in correlation between wind speed and buoyancy flux is expected because of the wind speed dependence of the buoyancy flux (i.e., the flux is proportional to u_* , which is proportional to U_{10N}). However, the hydrostatic pressure change across an SST front is directly related to the depth-averaged change in temperature across the front as described by O'Neill et al. (2010b). Therefore, the smaller increase may be due to the fact that the change in hydrostatic pressure is only proportional to T_{v*} (i.e., the scalar component of the buoyancy flux), which is proportional to ΔT_v . The smaller increase also suggests the change in pressure is fairly insensitive to the enhanced mechanical mixing (i.e., due to an increase in u_* and surface stress) across the front.

The increase of correlation with increasing temporal scale beyond 30 days in Figs. 9 and 10 is similar to that for wind–SST correlations seen in Fig. 8. A measurable temporal difference seen in Fig. 10 is that the maximum correlations between the direct thermal forcing and wind or thermal forcing and wind stress are observed at significantly shorter T , closer to 40 days rather than 60–70 days for SST. This shift to shorter T indicates that some fraction of the atmospheric thermal adjustment and resulting coherent wind speed perturbations occurs at slightly shorter space and time scales than for the results seen when using the SST gradient as the surrogate for controls (such as the pressure gradient force and heat flux). Coherency here may occur at longer scales, more in line with that seen for the pressure field perturbation in Fig. 10.

While the time-variant correlation coefficient results of Figs. 8, 9, and 10 provide some indication of the time (length) scales contributing to cross-frontal atmosphere–ocean coupling, an additional assessment may be found by computing the coherence spectra between U_{10N} and the thermal forcing variables, as shown in Fig. 11. The time series used to compute the coherence in this figure are unfiltered and span 12 months (November 2005–November 2006). The dashed line in Fig. 11 represents the limiting coherence squared at probability level $p = 0.1$ (Thompson 1979), where the time series have

necessarily been divided into 90-day segments using a Hanning window with 50% overlap in order to achieve sufficient signal to noise. This provides approximately 13 degrees of freedom. Although limited by the length of the data record and 90-day partitioning, the results do indicate consistency with the previous analyses. In particular, the coherence is again smallest between U_{10} and SST and largest between U_{10N} and the buoyancy flux. Moreover, the wind speed coherence with both ΔT_v and the buoyancy flux perturbations is significant (at $p = 0.1$) between periods of approximately 20 and 45 days, and the peak is at a measurably shorter frequency than that between SST and the wind.

To relate time and length scales, we suppose that regional ocean temperature variability is dominated by Gulf Stream meanders. Translating maximum values in T shown in Figs. 7–11 to regional spatial scales of correlation can be addressed using previous Gulf Stream instability wave studies (e.g., Hansen 1970; Halliwell and Mooers 1983; Lee and Cornillon 1996) that quantified the period, wavelength, and phase speed of these meanders. Halliwell and Mooers report phase speeds of the Gulf Stream meanders between $5\text{--}10\text{ cm s}^{-1}$ and wavelengths between 200 and 400 km. This is used to convert the period in Fig. 11 to wavelength, and this is shown as the top x -axis label using an average meander velocity of 7.5 cm s^{-1} . The statistically significant values of the coherence in Fig. 11 fall between 300 and 700 km, consistent with Lee and Cornillon (1996). Moreover, the results here show a shift toward longer scale for the SST–wind cospectrum similar to the differences observed in Figs. 8 and 9. Thus, at least for the CLIMODE site in 2006, the coupling observed represents air–sea interaction at a fairly long duration and length scales that are consistent with a secondary circulation process tied to north wall meanders.

4. Discussion and summary

Results from this study are, in many respects, consistent with and complementary to recent investigations that address the apparent coupling between near-surface wind and oceanic surface temperature gradients at 30-day and 200–300-km length scales (cf. Chelton et al. 2004; Small et al. 2008; O'Neill 2012). Salient components of this dataset include in situ relative wind speed (i.e., corrected for surface currents), atmospheric pressure, and air–sea fluxes of buoyancy and momentum. Somewhat surprisingly, time series analysis of data from a single fixed mooring yields a nearly linear coupling coefficient (Fig. 7) between temporal SST and wind speed perturbations about a 30-day running average that is in close agreement with results obtained by

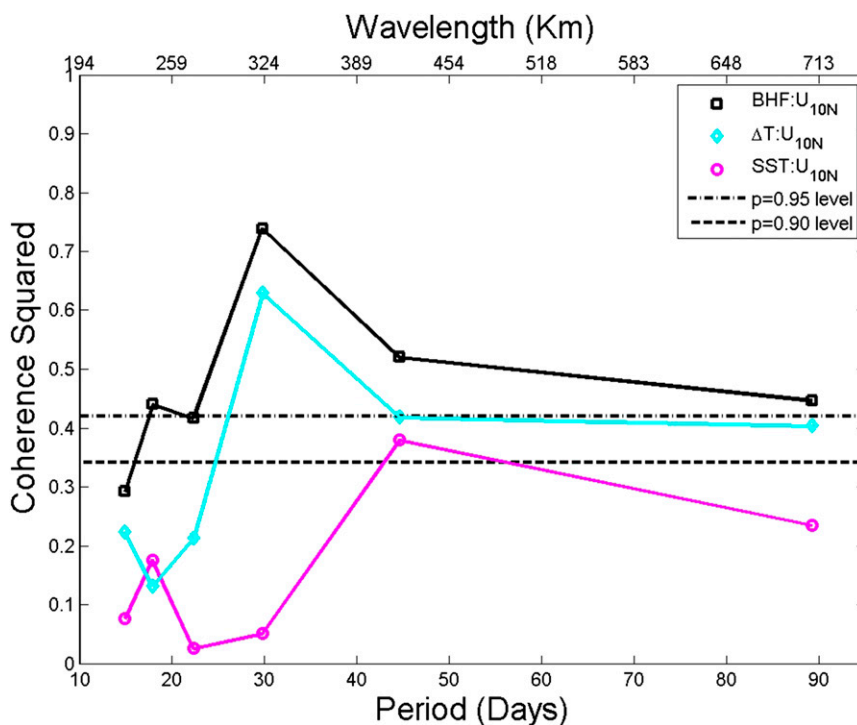


FIG. 11. Observed coherence squared coefficients as a function of period and wavelength. Duration has been converted to wavelength using a phase speed of 7.5 cm s^{-1} . The coherences between U_{10N} and SST, ΔT , and buoyancy flux are shown. The dashed line represents the limiting coherence squared at probability levels of $p = 0.90$ and 0.95 .

many investigations that find this relationship in observed horizontal spatial gradients (e.g., Xie et al. 1998; Chelton et al. 2001; Song et al. 2006). These studies have primarily been performed using satellite SST and wind data but also more recently using measurements between an extensive set of distant buoy pairs (O'Neill 2012). We performed a similar but more localized buoy-pairwise analysis to corroborate that work and to find an SST–wind coupling coefficient (0.19 ± 0.04) that is statistically identical to the average value for the NW Atlantic results obtained by O'Neill (2012). We thus conclude that the conditions surrounding this CLIMODE buoy site from 2005 to 2007 exhibit similar SST control of the winds. More critically, temporal variability in SST driven by Gulf Stream meanders and advection of smaller-scale gradients about the single CLIMODE station allow the buoy to sufficiently sample oceanic horizontal gradients and resulting air–sea coupling.

Using these data, we have come to several conclusions that augment previous work and provide further support for ongoing studies to attribute observed near-surface wind variation to controlling processes.

First, the data clearly show that cross-gradient wind adjustment due to atmospheric stability, as predicted by Monin–Obukhov similarity, is a contributing but not

dominant factor in the observed coupling between wind stress or ENW and SST. The increase observed in α_v for ENW versus the wind speed itself is found to be about 20%–30% (see Figs. 7 and 8). This increase is consistent with observations in O'Neill (2012) and also that predicted much earlier in the simulation of Wai and Stage (1989). Moreover, QuikSCAT satellite wind speed data, combined with the in situ flux measurements, show that the satellite winds are more closely related to wind speed adjusted to neutral conditions using MO similarity (i.e., ENW) than the actual (measured) wind speed (Fig. 3). Throughout the correlation analyses in section 5, results using the QuikSCAT wind are most congruous with the in situ U_{10N} . Thus, satellite winds can be interpreted to act like an ENW (O'Neill et al. 2012), and the dominant process in the wind coupling to the SST gradients is not surface layer adjustment.

Next, results of section 5 can be distilled to a few key findings. One is that the absolute value of the sensitivity between SST and wind α_v or wind stress α_τ varies depending on scale of the temporal variability. The time variation is controlled by the high-pass filter cutoff set by the running mean. Observed variation in α_v was 50%–80% (Fig. 8), with highest values near a time scale

of 60 days. The variation is consistent in magnitude with the interbasin geographical variability in α_v shown in O'Neill et al. (2012) using satellite data. That study also concluded that their data led to a regionwide value of α_v (0.30 ± 0.05) for the NW Atlantic that was significantly smaller than our observed maximum of 0.48 in this same region. Our α_v variation within this region is also larger. The data and the data analyses approaches are clearly not equivalent, but we do arrive at α_v and α_τ values similar to that work when using a time scale of 30 days. Those authors speculated that one reason for the as yet unexplained larger interbasin variability in α_v could be differences in large-scale ABL structure and coupling with the ocean. The present study shows averaging time scales and the variability in the horizontal scales of the ocean mesoscale features themselves may contribute.

Another finding is that the highest correlation with wind or wind stress perturbations is obtained with the variation in buoyancy heat flux (BHF), not the SST. The observed increase in explained variance is large. This result is not too surprising when one considers BHF depends on both u_* and the sea–air thermal forcing and that SST-induced heat flux gradients are central in all modeling to date surrounding this ocean–atmosphere phenomenon. Still, it is instructive to show through directly measured heat fluxes that this apparent linear SST–wind coupling, as observed for many years and in numerous studies, is indeed mediated through this thermal forcing.

A third finding is that anticorrelation with the pressure perturbations (Figs. 9, 10) confirms the fundamental expectation that surface level pressure change (due to hydrostatic adjustment with changing temperature) is involved in and consistent with the observed flow and overall dynamics. In effect, surface winds are enhanced over warmer water with lower pressure and suppressed over cooler water with higher pressure in part because of the resulting pressure gradient force.

Finally, the time-variable analyses among diagnostic variables indicates that the maximum impact of SST on wind as well as the pressure (Fig. 10) and BHF (not shown) is observed at slightly longer time scales [$O(60\text{--}70)$ days] than for the wind–BHF or sea–air temperature difference correlations. Moreover, we relate this former time scale to oceanic mesoscale variation of length 300–500 km, consistent with the previous works that identify the length scale of Gulf Stream instability fronts and meanders found near the north wall.

A summary result in Fig. 12 is provided to document coupling coefficients among the diagnostic variables that can be related to past and future numerical simulations dealing with surface level perturbations within these systems (cf. Wai and Stage 1989; Small et al. 2008;

O'Neill et al. 2010b). A high-pass filtering time scale of 60 days is used to correspond with the scale of strongest SST impact. Again, as in Fig. 10, the most prominent feature is the increase in the correlation coefficient as one moves from left to right in each row, indicating that the heat flux is fundamental in the system at a time scale of 60 days and less.

We believe this is one of the first studies to document surface pressure variation due to SST change in the Gulf Stream region. The observed coupling level of $-0.69 \text{ hPa}^\circ\text{C}^{-1}$ slightly exceeds that found in the tropical Pacific by Cronin et al. (2003) and in the Agulhas region numerical simulation of O'Neill et al. (2010b). But this higher value is consistent with what is predicted for the MABL height and temperatures found near the Gulf Stream (see Cronin et al. 2003). While not shown, the same term for buoyancy heat flux α_{bhf} is about $8 \text{ W m}^{-2}\text{C}^{-1}$ ($R = 0.49$). This is large and is likely to drive a strong thermally direct secondary flow based on the study results of O'Neill et al. (2010b), where values of $15 \text{ W m}^{-2}\text{C}^{-1}$ were predicted. This also agrees well with the values given in Wai and Stage (1989), a simulation examining the atmospheric response to a strong SST gradient using an idealized model over this Gulf Stream region. Together, these observations yield results consistent with modeling (e.g., Wai and Stage 1989; O'Neill et al. 2010b) that suggest the oceanic mesoscale SST gradients induce a secondary circulation via air–sea coupling, thermal forcing, and subsequent horizontal pressure adjustment that together control a near-surface wind gradient that varies somewhat linearly ($R = 0.3\text{--}0.45$) with the SST variation. This supports the third finding above that the observed wind perturbations were due to the formation of a horizontal pressure gradient driven by the adjustment of air temperature and humidity to the underlying SST at the oceanic mesoscale.

This study was not without limitations, central among them being the dependence on oceanic advection about the buoy, lack of any observations aloft to more fully examine processes such as the vertical stress profile and divergence, and the relatively short length of the measurement time series. The latter hindered the ability to examine results because of variation in the advective processes as a result of changes in wind direction relative to the SST front, as well as the possible seasonal variation in wind stress to SST coupling α_τ , such as that observed in O'Neill et al. (2012). Still, the dataset and study may provide some constructive information for future satellite or in situ efforts that wish, for example, to examine potential air–sea coupling at oceanic sub-mesoscale. In this event, it appears a fairly modest complement of instruments (e.g., a precise barometer and air and sea surface temperature sensors) on a few

Perturbations about 60 Day Running Average

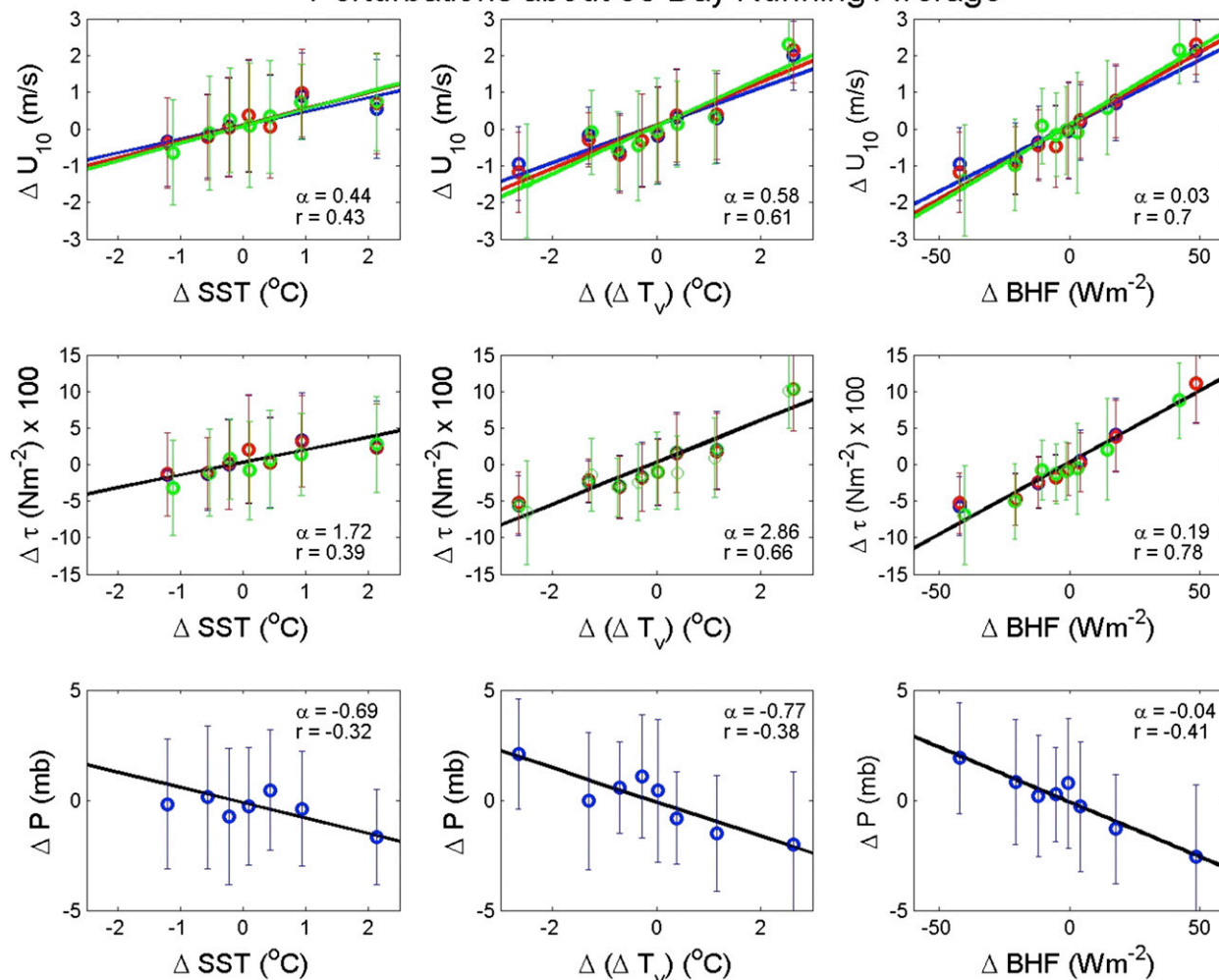


FIG. 12. A mosaic of the bin-averaged results and linear fit coupling and regression coefficients and for (top) U_{10N} , (middle) surface wind stress, and (bottom) surface pressure against perturbations in the thermal variables used in the analysis after removal of a 60-day running mean.

well-placed moorings or drifters may produce data to support refined understanding of the generation and maintenance of the air–sea coupling across such features.

Acknowledgments. We thank Jon Ware and Steve Faluotico (WHOI, AOPE) and the personnel of the Upper Ocean Processes group (WHOI-PO), who designed, calibrated, maintained, and deployed the components of the ASIT, ASIS, and surface mooring. Code for assessing statistical significance was provided by Melanie Fewings, Carlos Moffat, Mike Whitney, and Bob Beardsley. This research was supported by NASA Grant NNX10AO85G as part of NASA Ocean Vector Wind Science Team activities and by NSF Grant OCE04-24536 as part of the CLIMODE project. We thank numerous NASA ocean wind science team

members, particularly L. O’Neill, for helpful discussions related to formulating and refining the data analyses.

REFERENCES

- Bigorre, S., R. A. Weller, J. Lord, J. B. Edson, and J. D. Ware, 2013: A surface mooring for air–sea interaction research in the Gulf Stream. Part II: Analysis of the observations and their accuracies. *J. Atmos. Oceanic Technol.*, **30**, 450–469, doi:10.1175/JTECH-D-12-00078.1.
- Bourassa, M. A., S. T. Gille, D. L. Jackson, J. B. Roberts, and G. A. Wick, 2010: Ocean winds and turbulent air–sea fluxes inferred from remote sensing. *Oceanography*, **23**, 36–51, doi:10.5670/oceanog.2010.04.
- Chelton, D. B., 1983: Effects of sampling errors in statistical estimation. *Deep-Sea Res.*, **30**, 1083–1103, doi:10.1016/0198-0149(83)90062-6.
- , and S.-P. Xie, 2010: Coupled ocean–atmosphere interaction at oceanic mesoscale. *Oceanography*, **23**, 52–69, doi:10.5670/oceanog.2010.05.

- , and Coauthors, 2001: Observations of coupling between surface wind stress and sea surface temperature in the eastern tropical Pacific. *J. Climate*, **14**, 1479–1498, doi:10.1175/1520-0442(2001)014<1479:OOCBSW>2.0.CO;2.
- , M. G. Schlax, M. H. Freilich, and R. F. Milliff, 2004: Satellite measurements reveal persistent small-scale features in ocean winds. *Science*, **303**, 978–983, doi:10.1126/science.1091901.
- Colton, M. C., W. J. Plant, W. C. Keller, and G. L. Geernaert, 1995: Tower-based measurements of normalized radar cross section from Lake Ontario: Evidence of wind stress dependence. *J. Geophys. Res.*, **100**, 8791–8813, doi:10.1029/95JC00364.
- Cronin, M. F., S.-P. Xie, and H. Hashizume, 2003: Barometric pressure variations associated with eastern Pacific tropical instability waves. *J. Climate*, **16**, 3050–3057, doi:10.1175/1520-0442(2003)016<3050:BPVAWE>2.0.CO;2.
- Ebuchi, N., H. C. Graber, and M. J. Caruso, 2002: Evaluation of wind vectors observed by QuikSCAT/SeaWinds using ocean buoy data. *J. Atmos. Oceanic Technol.*, **19**, 2049–2062, doi:10.1175/1520-0426(2002)019<2049:EOWVOB>2.0.CO;2.
- Edson, J. B., and C. W. Fairall, 1998: Similarity relationships in the marine atmospheric surface layer for terms in the TKE and scalar variance budgets. *J. Atmos. Sci.*, **55**, 2311–2328, doi:10.1175/1520-0469(1998)055<2311:SRITMA>2.0.CO;2.
- , A. A. Hinton, K. E. Prada, J. E. Hare, and C. W. Fairall, 1998: Direct covariance flux estimates from mobile platforms at sea. *J. Atmos. Oceanic Technol.*, **15**, 547–562, doi:10.1175/1520-0426(1998)015<0547:DCFEFM>2.0.CO;2.
- , C. J. Zappa, J. A. Ware, W. R. McGillis, and J. E. Hare, 2004: Scalar flux profile relationships over the open ocean. *J. Geophys. Res.*, **109**, C08S09, doi:10.1029/2003JC001960.
- , and Coauthors, 2013: On the exchange of momentum over the open ocean. *J. Phys. Oceanogr.*, **43**, 1589–1610, doi:10.1175/JPO-D-12-0173.1.
- Emery, W. J., and R. E. Thomson, 2001: *Data Analysis Methods in Physical Oceanography*. Elsevier Science, 638 pp.
- Fairall, C. W., E. F. Bradley, D. P. Rogers, J. B. Edson, and G. S. Young, 1996: Bulk parameterization of air–sea fluxes for Tropical Ocean-Global Atmosphere Coupled-Ocean Atmosphere Response Experiment. *J. Geophys. Res.*, **101**, 3747–3764, doi:10.1029/95JC03205.
- , —, J. E. Hare, A. A. Grachev, and J. B. Edson, 2003: Bulk parameterization of air–sea fluxes: Updates and verification for the COARE algorithm. *J. Climate*, **16**, 571–591, doi:10.1175/1520-0442(2003)016<0571:BPOASF>2.0.CO;2.
- Freilich, M., and R. Dunbar, 1999: The accuracy of the NSCAT 1 vector winds: Comparisons with National Data Buoy Center buoys. *J. Geophys. Res.*, **104**, 11 231–11 246, doi:10.1029/1998JC000091.
- Halliwell, G. R., and C. N. K. Mooers, 1983: Meanders of the Gulf Stream downstream from Cape Hatteras 1975–1978. *J. Phys. Oceanogr.*, **13**, 1275–1292, doi:10.1175/1520-0485(1983)013<1275:MOTGSD>2.0.CO;2.
- Hansen, D. V., 1970: Gulf Stream meanders between Cape Hatteras and the Grand Banks. *Deep-Sea Res.*, **17**, 495–511, doi:10.1016/0011-7471(70)90064-1.
- Hosom, D. S., R. A. Weller, R. E. Payne, and K. E. Prada, 1995: The IMET (improved meteorology) ship and buoy systems. *J. Atmos. Oceanic Technol.*, **12**, 527–540, doi:10.1175/1520-0426(1995)012<0527:TIMSAB>2.0.CO;2.
- Kelly, K. A., S. Dickinson, M. J. McPhaden, and G. C. Johnson, 2001: Ocean currents evident in satellite wind data. *Geophys. Res. Lett.*, **28**, 2469–2472, doi:10.1029/2000GL012610.
- Larsen, S. E., J. B. Edson, C. W. Fairall, and P. G. Mestayer, 1993: Measurement of temperature spectra by a sonic anemometer. *J. Atmos. Oceanic Technol.*, **10**, 345–354, doi:10.1175/1520-0426(1993)010<0345:MOTSBA>2.0.CO;2.
- Lee, T., and P. Cornillon, 1996: Propagation and growth of Gulf Stream meanders between 75° and 45°W. *J. Phys. Oceanogr.*, **26**, 225–241, doi:10.1175/1520-0485(1996)026<0225:PAGOGS>2.0.CO;2.
- Liu, W. T., and W. Tang, 1996: Equivalent neutral wind. Jet Propulsion Laboratory Tech. Rep. 96-17, 22 pp. [Available online at <http://ntrs.nasa.gov/archive/nasa/casi.ntrs.nasa.gov/19970010322.pdf>.]
- Marshall, J., and Coauthors, 2009: The CLIMODE field campaign: Observing the cycle of convection and restratification over the Gulf Stream. *Bull. Amer. Meteor. Soc.*, **90**, 1337–1350, doi:10.1175/2009BAMS2706.1.
- Miller, S., C. Friehe, T. Hristov, and J. Edson, 2008: Platform motion effects on measurements of turbulence and air–sea exchange over the open ocean. *J. Atmos. Oceanic Technol.*, **25**, 1683–1694, doi:10.1175/2008JTECHO547.1.
- NOAA/National Data Buoy Center, 2012: Historical standard meteorological station data. [Available online at <http://www.ndbc.noaa.gov/data/>.]
- O’Neill, L. W., 2012: Wind speed and stability effects on coupling between surface wind stress and SST observed from buoys and satellite. *J. Climate*, **25**, 1544–1569, doi:10.1175/JCLI-D-11-00121.1.
- , D. B. Chelton, and S. K. Esbensen, 2003: Observations of SST-induced perturbations of the wind stress field over the Southern Ocean on seasonal timescales. *J. Climate*, **16**, 2340–2354, doi:10.1175/2780.1.
- , —, —, and F. J. Wentz, 2005: High-resolution satellite measurements of the atmospheric boundary layer response to SST variations along the Agulhas Return Current. *J. Climate*, **18**, 2706–2723, doi:10.1175/JCLI3415.1.
- , —, and —, 2010a: The effects of SST-induced surface wind speed and direction gradients on midlatitude surface vorticity and divergence. *J. Climate*, **23**, 255–281, doi:10.1175/2009JCLI2613.1.
- , S. K. Esbensen, N. Thum, R. M. Samuelson, and D. B. Chelton, 2010b: Dynamical analysis of the boundary layer and surface wind responses to mesoscale SST perturbations. *J. Climate*, **23**, 559–581, doi:10.1175/2009JCLI2662.1.
- , D. B. Chelton, and S. K. Esbensen, 2012: Covariability of surface wind and stress responses to sea surface temperature fronts. *J. Climate*, **25**, 5916–5942, doi:10.1175/JCLI-D-11-00230.1.
- Park, K.-A., P. C. Cornillon, and D. L. Codiga, 2006: Modification of surface winds near ocean fronts: Effects of Gulf Stream rings on scatterometer (QuikSCAT, NSCAT) wind observations. *J. Geophys. Res.*, **111**, C03021, doi:10.1029/2005JC003016.
- Perlin, N., S. P. de Zoete, D. B. Chelton, R. M. Samuelson, E. D. Skyllinstad, and L. W. O’Neill, 2014: On scatterometer ocean stress. *Mon. Wea. Rev.*, **142**, 4284–4307, doi:10.1175/MWR-D-13-00332.1.
- Pineda, J., and M. Lopez, 2002: Temperature, stratification and barnacle larval settlement in two Californian sites. *Cont. Shelf Res.*, **22**, 1183–1198, doi:10.1016/S0278-4343(01)00098-X.
- Plagge, A. M., D. C. Vandemark, and D. G. Long, 2009: Coastal validation of ultra-high resolution wind vector retrieval from QuikSCAT in the Gulf of Maine. *IEEE Geosci. Remote Sens. Lett.*, **6**, 413–417, doi:10.1109/LGRS.2009.2014852.

- , —, and B. Chapron, 2012: Examining the impact of surface currents on satellite scatterometer and altimeter ocean winds. *J. Atmos. Oceanic Technol.*, **29**, 1776–1793, doi:10.1175/JTECH-D-12-00017.1.
- Quilfen, Y., B. Chapron, and D. Vandemark, 2001: The ERS scatterometer wind measurement accuracy: Evidence of seasonal and regional biases. *J. Atmos. Oceanic Technol.*, **18**, 1684–1697, doi:10.1175/1520-0426(2001)018<1684:TESWMA>2.0.CO;2.
- Ross, D. B., V. J. Cardone, J. Overland, R. D. McPherson, W. J. Pierson, and T.-W. Yu, 1985: Ocean surface winds. *Adv. Geophys.*, **27**, 101–140, doi:10.1016/S0065-2687(08)60404-5.
- SeaPAC, 2013: QuikSCAT Level 2B ocean wind vectors in 12.5 km slice composites version 3. PO.DAAC, doi:10.5067/QSX12-L2B01.
- Schneider, N., and B. Qiu, 2015: The atmospheric response to weak sea surface temperature fronts. *J. Atmos. Sci.*, **72**, 3356–3377, doi:10.1175/JAS-D-14-0212.1.
- Small, R. J., and Coauthors, 2008: Air–sea interaction over ocean fronts and eddies. *Dyn. Atmos. Oceans*, **45**, 274–319, doi:10.1016/j.dynatmoce.2008.01.001.
- Smith, S. D., 1988: Coefficients for sea surface wind stress, heat flux, and wind profiles as a function of wind speed and temperature. *J. Geophys. Res.*, **93**, 15 467–15 472, doi:10.1029/JC093iC12p15467.
- Song, Q., P. Cornillon, and T. Hara, 2006: Surface wind response to oceanic fronts. *J. Geophys. Res.*, **111**, C12006, doi:10.1029/2006JC003680.
- Spall, M. A., 2007: Midlatitude wind stress–sea surface temperature coupling in the vicinity of oceanic fronts. *J. Climate*, **20**, 3785–3801, doi:10.1175/JCLI4234.1.
- Thompson, R. O. R. Y., 1979: Coherence significance levels. *J. Atmos. Sci.*, **36**, 2020–2021, doi:10.1175/1520-0469(1979)036<2020:CSL>2.0.CO;2.
- Verschell, M., M. Bourassa, D. Weissman, and J. O'Brien, 1999: Ocean model validation of the NASA scatterometer winds. *J. Geophys. Res.*, **104**, 11 359–11 373, doi:10.1029/1998JC900105.
- Wai, M., and S. A. Stage, 1989: Dynamical analysis of marine atmospheric boundary layer structure near the Gulf Stream oceanic front. *Quart. J. Roy. Meteor. Soc.*, **115**, 29–44, doi:10.1002/qj.49711548503.
- Weissman, D. E., 1990: Dependence of the microwave radar cross section on ocean surface variables: Comparison of measurements and theory using data from the Frontal Air–Sea Interaction Experiment. *J. Geophys. Res.*, **95**, 3387–3398, doi:10.1029/JC095iC03p03387.
- , and H. Graber, 1999: Satellite scatterometer studies of ocean surface stress and drag coefficients using a direct model. *J. Geophys. Res.*, **104**, 11 329–11 335, doi:10.1029/1998JC900117.
- , and Coauthors, 1997: Measurements of ocean surface stress using aircraft scatterometers. *J. Atmos. Oceanic Technol.*, **14**, 835–848, doi:10.1175/1520-0426(1997)014<0835:MOOSSU>2.0.CO;2.
- Weller, R. A., S. P. Bigorre, J. Lord, J. D. Ware, and J. B. Edson, 2012: A surface mooring for air–sea interaction research in the Gulf Stream. Part I: Mooring design and instrumentation. *J. Atmos. Oceanic Technol.*, **29**, 1363–1376, doi:10.1175/JTECH-D-12-00060.1.
- Whitney, M. M., and R. W. Garvine, 2006: Simulating the Delaware Bay buoyant outflow: Comparison with observations. *J. Phys. Oceanogr.*, **36**, 3–21, doi:10.1175/JPO2805.1.
- Xie, S.-P., M. Ishiwatari, H. Hashizume, and K. Takeuchi, 1998: Coupled ocean–atmosphere waves on the equatorial front. *Geophys. Res. Lett.*, **25**, 3863–3866, doi:10.1029/1998GL900014.
- Zhang, R.-H., and A. J. Busalacchi, 2009: An empirical model for surface wind stress response to SST forcing induced by tropical instability waves (TIWs) in the eastern equatorial Pacific. *Mon. Wea. Rev.*, **137**, 2021–2046, doi:10.1175/2008MWR2712.1.